# Modeling Study of the Effects of Membrane Surface Charge on Calcium Microdomains and Neurotransmitter Release

Luigi Catacuzzeno, Bernard Fioretti, and Fabio Franciolini
Dipartimento di Biologia Cellulare e Ambientale, Università di Perugia, Perugia, Italy

ABSTRACT Synchronous neurotransmitter release is mediated by the opening of voltage-gated $Ca^{2+}$ channels and the build-up of submembrane $Ca^{2+}$ microdomains. Previous models of $Ca^{2+}$ microdomains have neglected possible electrostatic interactions between $Ca^{2+}$ ions and negative surface charges on the inner leaflet of the plasma membrane. To address the effects of these interactions, we built a computational model of ion electrodiffusion described by the Nernst-Planck and Poisson equations. We found that inclusion of a negative surface charge significantly alters the spatial characteristics of $Ca^{2+}$ microdomains. Specifically, close to the membrane, $Ca^{2+}$ ions accumulate, as expected from the strong electrostatic attraction exerted on positively charged $Ca^{2+}$ ions. Farther away from the membrane, increasing the surface charge density results in a reduction of the $Ca^{2+}$ concentration because of the preferential spread of $Ca^{2+}$ ions along lateral directions. The model also predicts that the negative surface charge will decrease the spatial gradient of the $Ca^{2+}$ microdomain in the lateral direction, resulting in increased overlap of microdomains originating from different $Ca^{2+}$ channels. Finally, we found that surface charge increases the probability of vesicle release if the $Ca^{2+}$ sensor is located within the electrical double layer, whereas this probability is decreased if the $Ca^{2+}$ sensor lies at greater distances from the membrane. Our data suggest that membrane surface charges exert a significant influence on the profile of $Ca^{2+}$ microdomains, and should be taken into account in models of neurotransmitter release.

## INTRODUCTION

The entry of $Ca^{2+}$ ions through voltage-gated $Ca^{2+}$ channels is necessary for triggering vesicle fusion and neurotransmitter release (1,2). Electron microscopy studies of vertebrate synapses provide strong evidence for strict colocalization between synaptic vesicles and transmembrane particles, thought to be $Ca^{2+}$ channels, with an estimated channel-vesicle distance of ~10–30 nm (3). Several studies point to a direct physical and functional interaction between voltage-gated $Ca^{2+}$ channels and several vesicle-associated proteins implicated in neurotransmitter release (3–5). Because of the limited rate of diffusion of $Ca^{2+}$ ions within the cytoplasm and small $Ca^{2+}$ channel-vesicle distances, the $Ca^{2+}$ concentration ([Ca]) at the sensor protein is thought to attain levels much higher than those present in the bulk. Due to the small spatial scale of these $Ca^{2+}$ signals ($Ca^{2+}$ microdomains), it has been impossible thus far to investigate their properties experimentally by direct $Ca^{2+}$ imaging. Therefore, information regarding their shape and dynamics has remained elusive.

Theoretical modeling is thus the only viable approach for making inferences about the detailed properties of the $Ca^{2+}$ microdomains and their linkage to neurotransmitter release. Computer simulations of $Ca^{2+}$ microdomains, based essentially on Fick's law of diffusion, have demonstrated that at a few tens of nanometers from an open $Ca^{2+}$ channel, where the sensor protein is supposedly located, the [Ca] reaches levels >100 $\mu$M (6–8). In addition, the predicted [Ca] profiles show steep spatial gradients, such that within several hundred nanometers from the channel the enhanced [Ca] level has decreased to near bulk levels. Because of the steep $Ca^{2+}$ microdomain gradients, these models predict that release of a docked vesicle would be mainly controlled by the colocalized $Ca^{2+}$ channel, even in the presence of other $Ca^{2+}$ channels located farther away from the vesicle (9,10).

Although some functional data, such as those derived from lower vertebrate synapses, essentially support these theoretical predictions (11–13), recent results on the mammalian calyx of Held and cortical synapses seem to suggest a different scenario (14,15). First, at the release $Ca^{2+}$ sensor of the rat calyx of Held, a much smaller [Ca] (10–25 $\mu$M) was found to be sufficient to achieve both the amount and the kinetics of the transmitter release under physiological conditions (1,16). Second, experiments aimed at evaluating the sensitivity of neurotransmitter release to $Ca^{2+}$ channel blockers and fast $Ca^{2+}$ buffers indicate that remote $Ca^{2+}$ channels may also contribute to the fusion of a single vesicle, with some of them possibly being as far as 100 nm from the release $Ca^{2+}$ sensor (16,17). These recent observations cannot be reproduced by theoretical models that assume a strong colocalization between $Ca^{2+}$ channels and release vesicles, as the structural evidence suggests (9). Alternatives include consideration of a less strict channel-vesicle colocalization at the Calyx of Held synapse in the rat (9). However, conclusions about $Ca^{2+}$ channel-vesicle topography based on interpretation of available functional data strongly rely on the validity of the employed theoretical models of $Ca^{2+}$ microdomains. These should take into account all the relevant physical processes or parameters necessary to give a correct prediction of the [Ca] profile near an open $Ca^{2+}$ channel.

*Submitted November 4, 2007, and accepted for publication May 5, 2008.*

Address reprint requests to Luigi Catacuzzeno, Dipartimento di Biologia Cellulare e Ambientale, Università di Perugia, via Pascoli 1, I-06123 Perugia, Italy. E-mail: fabiolab@unipg.it.

Editor: Robert Hsiu-Ping Chow.


0006-3495/08/09/2160/12 $2.00

doi: 10.1529/biophysj.107.124909

One potentially relevant factor that has not been incorporated into existing models of $Ca^{2+}$ microdomains and neurotransmitter release is electrostatic force, which could markedly influence the distribution of $Ca^{2+}$ ions within the cell. It is known that the inner leaflet of mammalian plasma membrane carries a significant negative charge due to the negatively charged phospholipid headgroups and amino acids of membrane proteins facing the cytoplasm (18,19). In addition recent studies suggest that phosphoinositides, carrying a substantial negative headgroup charge, concentrate at the presynaptic active zones (20,21), raising the possibility that the negative surface charge density at release sites may well be even higher than in other regions of the plasma membrane. It is also established that these negative charges generate a negative electrostatic potential that persists for several nanometers within the electrolytic solution bathing the membrane. This negative potential will attract cations and repel anions, and will have an impact on the distribution of ions in the immediate vicinity.

In this article, we explore a possible role of membrane surface charges in shaping the $Ca^{2+}$ microdomain around an open $Ca^{2+}$ channel. This has been achieved by using a computational model that calculates the ionic concentration profiles and the electrostatic potential near the membrane, in the presence of $Ca^{2+}$ influx. We have also tested how the changes in the $Ca^{2+}$ microdomain properties induced by membrane surface charges will reflect on the $Ca^{2+}$-dependent neurotransmitter release. Our results indicate that surface charges make a tangible contribution toward shaping $Ca^{2+}$ microdomains, thus changing the predicted neurotransmitter release.

## THEORY

### The model

Our model consists of a flat plasma membrane bathed by an electrolytic aqueous solution. The negative charges at the surface of the membrane, mainly due to phospholipid headgroups, are represented as a uniformly smeared negative surface charge density, $\sigma_T$, which in our calculations varies up to $-0.1$ C/m$^2$, a value within the range experimentally determined for the inner leaflet of plasma membranes (19). Theoretical Poisson-Boltzmann calculations indicate that the approximation of discrete membrane charges with a uniformly smeared membrane charge has realistic consequences in the assessed profile of the electrostatic potential, at least for physiologically relevant membrane phospholipid compositions (22). The plasma membrane also contains one or more $Ca^{2+}$ channels through which $Ca^{2+}$ ions can enter the electrolytic solution at a rate that depends on the unitary $Ca^{2+}$ current, $i_{Ca}$. The solution in contact with the membrane contains $K^+$, $Ca^{2+}$, $Mg^{2+}$, and $Cl^-$ ions in addition to a mobile buffer, $B^{2-}$, that binds $Ca^{2+}$ ions in accordance with the following 1:1 reaction scheme

$$B^{2-} + Ca^{2+} \underset{k_{-1}}{\overset{k_1}{\rightleftarrows}} CaB, \qquad \text{(Scheme 1)}$$

where CaB represents the buffer molecule bound to $Ca^{2+}$, and $k_1$ and $k_{-1}$ are the $Ca^{2+}$ binding and unbinding rate constants. In our calculations, the species concentrations at the bulk (very far from the membrane) are as follows. The concentration of free (unbound) $Ca^{2+}$, $[Ca]_{bulk}$, is $10^{-7}$ M; the concentration of free buffer, [B], is settled according to the following equilibrium condition for scheme 1:

$$[B] = \frac{k_{-1}B_T}{k_1[Ca] + k_{-1}}, \qquad (1)$$

where $B_T$, the total buffer concentration, is considered to be 0.5 mM. The concentration of the $Ca^{2+}$-bound buffer, [BCa], is ($B_T$-[B]); the concentration of $K^+$, [K], is set to 0.14 M + 2[B]; the concentration of $Mg^{2+}$, [Mg], is set to 0.5 mM. Last, the concentration of $Cl^-$ ions, [Cl], chosen to ensure electroneutrality, is 0.14 M + 2 [Ca] + 2 [Mg]. Since in our computations we considered only the steady-state [Ca] profile, immobile buffers can be neglected, since their tendency to saturate does not allow any significant contribution (23).

### The flux conservative equation

The concentration profiles near the membrane are calculated by solving the flux conservative equation, applied to each ion present in the electrolytic solution. We considered the steady-state form of the flux conservative equation, which for ion $j$ reads

$$\nabla f_j + F_j = 0. \qquad (2)$$

The term $f_j$ represents the flux of particle $j$ due to electrodiffusion. Following Nernst and Planck, we describe the electrodiffusional flow by

$$f_j = -D_j\left[\nabla C_j + \frac{z_j F}{RT} C_j \nabla V\right], \qquad (3)$$

where $D_j$ is the diffusion coefficient of ion $j$, $C_j$ is its concentration, and $z_j$ its valence; $F$ is the Faraday constant, $R$ is the gas constant, $T$ is the absolute temperature and V is the electrostatic potential. Equation 3 contains two additive terms, each having its own physical meaning. The first term describes the motion of particles through a concentration gradient $\nabla C_j$, according to Fick's first law of diffusion. The second term accounts for the drift velocity of a charged particle, induced by the electric field $-\nabla V$.

The term $F_j$ in Eq. 2 accounts for changes in particle concentration due to chemical reactions. In our model, the only chemical reaction considered is the binding of $Ca^{2+}$ to the mobile $Ca^{2+}$ buffer (Scheme 1). Accordingly, $F_j = k_1$ [Ca] [B] $-k_{-1}$ [CaB] when $j$ represents either $Ca^{2+}$ or $B^{2-}$ and $F_j = k_{-1}$ [CaB] $-k_1$ [Ca] [B] when $j$ represents CaB. For the other species present in solution, $F_j = 0$.

### The Poisson equation

In our model, most of the particles residing in the electrolytic solution possess a charge. Their concentration profiles will thus be also determined by the electrostatic potential, $V$, according to Eq. 3. The value of $V$ is determined by considering all the charges present in the system, including the charged particle in the electrolytic solution and the surface charge on the membrane, by solving the following Poisson equation

$$\nabla^2 V = -\frac{F\sum_j C_j z_j}{\varepsilon\varepsilon_0}, \qquad (4)$$

where $C_j$ is the ion concentration of species $j$, $z_j$ is its valence, $F$ is the Faraday constant, $\varepsilon_0$ is the permittivity of vacuum, and $\varepsilon$ is the relative permittivity of water, considered to be 80. In Eq. 4, $j$ extends over all ion species present in the electrolytic solution. Notice that Eq. 4 does not take into account the negative surface charge present on the membrane, $\sigma$. The contribution of $\sigma$ to the electrostatic potential will be introduced by the following Neumann boundary condition, imposed at the interphase between the membrane and the electrolytic solution

$$\nabla_\perp V = -\frac{\sigma}{\varepsilon\varepsilon_0}, \qquad (5)$$

where $\nabla_\perp$ is the gradient normal to the membrane surface.

## Binding of cations to the membrane surface charges

It is well known that monovalent and divalent cations present in the solution can bind to negatively charged phospholipids, reducing the effective surface charge density, $\sigma$. The term ''binding'' is here used to describe interactions between ions and phospholipids that exceed those made through the mean electrostatic field. Following the work of McLaughlin et al. (18), we assume that $K^+$ ions bind to the negatively charged phospholipids $P^-$ according to the scheme

$$K^+ + P^- \rightleftarrows PK, \qquad \text{(Scheme 2)}$$

characterized by the association constant $K_1 = \{KP\}/(\{P^-\}[K])$, where the braces denote surface concentrations. Similarly, divalent $Ca^{2+}$ and $Mg^{2+}$ ions can bind to negative phospholipids according to the scheme (here shown for $Ca^{2+}$)

$$Ca^{2+} + P^- \rightleftarrows CaP^+, \qquad \text{(Scheme 3)}$$

which has association constants $K_2 = \{CaP\}/(\{P^-\}[Ca])$ for $Ca^{2+}$ binding, and $K_3 = \{MgP\}/(\{P^-\}[Mg])$ for $Mg^{2+}$ binding. Considering that the total surface charge density $\sigma_T$ is given by $-F\{P^-\}$, the equilibrium surface charge density will be given by

$$\sigma = \sigma_T \frac{1 - K_2[Ca] - K_3[Mg]}{1 + K_1[K] + K_2[Ca] + K_3[Mg]}, \qquad (6)$$

where [Ca], [Mg], and [K] refer to the concentrations adjacent to the membrane surface. In our model, we considered $K_1 = 0.15\ M^{-1}$, $K_2 = 12\ M^{-1}$, and $K_3 = 6\ M^{-1}$ assessed for ion binding to phosphatidylserine-containing membranes (18,24).

## Computational implementation

The system to be solved consists of coupled partial differential equations, namely, the flux conservative equation for each mobile species (Eq. 2) and the Poisson equation of electrostatics (Eq. 4). Individually, each of these equations was solved using a finite-difference approach, and implementing the successive over-relaxation method described in Press et al. (25). The solution of the overall system was found by applying the following iterative scheme, similar to that applied for the solution of the same set of equations in calculations of ion channel permeation (PNP theory (26)).

1. Starting from an initial estimate for the ion concentration profiles, the effective surface charge density is assessed using Eq. 6.
2. A new electrostatic potential profile is found by using the Poisson equation (Eq. 4). As stated above, this solution was obtained by the successive overelaxation method, using the following criterion to stop the iteration: $(F/RT) \times (V^{new} - V^{old}) < 10^{-9}$, where $V^{new}$ and $V^{old}$ are the $V$ values found at two successive iterations.
3. The newly computed electrostatic potential is then used to solve the flux conservative equation for each ion species (Eq. 2). We used a successive over-relaxation scheme, as described in Cardenas et al. (27), with a tolerance of $10^{-9}$. Because of the $Ca^{2+}$ buffering reaction, the flux conservative equations for $Ca^{2+}$, $B^{2-}$, and CaB species are coupled. At each iteration, the concentration profile for these particles was assessed using the previously determined concentration profiles for the other two species.
4. The relative change in the concentration of each ion species and electrostatic potential is assessed. If these values are all $<10^{-7}$, the iteration halts; otherwise, a new iteration is started.

We found that this iterative scheme was stable provided that the Poisson equation solved at each iteration was modified as (28)

$$\nabla^{*2}\varphi = -\sum_j z_j C_j + \left(\sum_j z_j^2 C_j\right)(\varphi^{new} - \varphi^{old}). \qquad (7)$$

Equation 7 is derived from Eq. 4 by making nondimensional the spatial variable (dividing by $d = 0.1$ Å), the electrostatic potential (dividing by $RT/F$), and the ion concentrations (multiplying by $F^2d^2/(\varepsilon\varepsilon_0 RT)$). In addition, the second term on the righthand side of Eq. 7 has been added. Since this term is zero when the solution of the system is reached ($\phi^{new} = \phi^{old}$), it does not influence the final output of the computation. However, during the iterative scheme, this term dampens the oscillatory behavior of the electrostatic potential, making the iteration stable.

For each condition tested, we first solved the ion concentration profiles and electrostatic potential in the absence of $Ca^{2+}$ influx. Due to the symmetry of the system in all directions parallel to the membrane, this solution was found by applying the iterative scheme described above to one-dimensional versions of Eqs. 2 and 4, which describe the spatial profiles of the variables along the $z$-direction, normal to the membrane. To find this solution, the following boundary conditions were used: for the flux conservative equation, $f$ at $z = 0$ (at the membrane) was settled to zero (reflective boundary condition), whereas at the other extreme (very far from the membrane), the ion concentrations were fixed to their given bulk values. In the Poisson equation, at $z = 0$, $dV/dz = -\sigma/\varepsilon\varepsilon_0$, and at $z = L$, $V = 0$. The concentration and potential profiles found under these equilibrium conditions were then used as starting values for the subsequent two- or three-dimensional computations made in the presence of $Ca^{2+}$ influx. In this case, the following boundary conditions were used: for the flux conservative equation, $f_j = 0$ at $z = 0$ everywhere and for all ion species. At the $Ca^{2+}$ channel location, $f_{Ca} = -i_{Ca}/(z_{Ca}FA)$, where $A$ is the area of the membrane facing the computational box containing the channel. At the other boundaries, ion concentrations were fixed to their equilibrium values, as determined from the previous one-dimensional computation. For the Poisson equation, $dV/dz = -\sigma/\varepsilon\varepsilon_0$ at the membrane, whereas at the other boundaries, $V$ was fixed to the equilibrium value, found in the one-dimensional computation.

Depending on the number of $Ca^{2+}$ channels present in the membrane, we used either two- or three-dimensional versions of Eqs. 2 and 4. In the presence of only one open $Ca^{2+}$ channel, the system has cylindrical symmetry, allowing its solution on a two-dimensional grid, including a $z$ direction normal to the membrane and an $r$ direction parallel to the membrane, and expressing the distance from the $Ca^{2+}$ channel. The minimum grid-element size had a width ($\Delta r$) of 0.01 nm and a height ($\Delta z$) of 0.01 nm, with its origin centered at the channel site. The dimensions of each adjacent grid element were increased by increasing $\Delta r$ by 20% in the $r$ direction, and $\Delta z$ by 20% in the $z$ direction. The computational box had a total dimension of 1.36 $\mu$m in both the $z$ and $r$ directions, and was composed of a total of $56 \times 56$ grid elements. We verified that reducing the size of the computational grids and assuming constantly spaced elements did not appreciably change the solution.

In the presence of more than one $Ca^{2+}$ channel, the system loses its cylindrical symmetry. Therefore, in this case, we used a three-dimensional version of Eqs. 2 and 4, solved along the $x$ and $y$ directions parallel to the membrane, and the $z$ direction normal to the membrane. The dimensions of the grid elements were settled in the following way. $\Delta z$ had the same values used in the two-dimensional computations, whereas the values of $\Delta x$ and $\Delta y$ had values of 256, 128, 64, 32, 16, 8, 4, 2, 1, 2, 4, 8, 4, 2, 1, 2, 4, 8, 4, 2, 1, 2, 4, 8, 16, 32, 64, 128, and 256 nm. The computational box had a total dimension of 1.031 $\mu$m in both the $x$ and $y$ directions, and 1.36 $\mu$m in the $z$ direction, and was composed of a total of 14,297 grid elements. The six $Ca^{2+}$ channels were placed in correspondence with the grid elements having $\Delta x = \Delta y = 1$ nm in contact with the membrane.

## Numerical tests

To check the accuracy of the code, we tested our output against several limiting cases for which analytical solutions exist. We first tested the Poisson equation and the flux conservative equation of our two-dimensional code separately. The Poisson equation was tested by considering a system containing no ions in solution and a flat charged membrane at $z = 0$, by imposing $V = 0$ at the computational grids farther from the membrane. For this system, the analytical solution for the electrostatic potential profile is

$$V(z) = \frac{\sigma}{\varepsilon\varepsilon_0}(L - x). \quad (8)$$

Fig. 1 *A* shows that our code accurately reproduced this solution.

The two-dimensional flux conservative equation was tested by computing the [Ca] profile in the presence of an open $Ca^{2+}$ channel, in the absence of $Ca^{2+}$ buffers, and not considering electrostatics. The analytical solution of this system is

$$[\mathrm{Ca}](r) = -\frac{i_{\mathrm{Ca}}}{2\pi DzFr} + C_0, \quad (9)$$

where $[\mathrm{Ca}](r)$ is the [Ca] at the radial distance, $r$, from the $Ca^{2+}$ channel, and $C_0$ is the bulk [Ca]. As shown in Fig. 1 *B*, the [Ca] profile assessed by our code was essentially identical to that predicted by Eq. 9. The two-dimensional flux conservative equation was also tested for the case of $Ca^{2+}$ influx from a $Ca^{2+}$ channel in the presence of a relatively high concentration of $Ca^{2+}$ buffer (10 mM). In this case, buffer saturation is irrelevant, and the [Ca] radial profile can be expressed as

$$[\mathrm{Ca}](r) = -\frac{i_{\mathrm{Ca}}}{2\pi DzFr} e^{-r/\lambda} + C_0, \quad (10)$$

with $\lambda = \sqrt{\dfrac{D}{k_1[B]}}$.

Fig. 1 *B* shows that in this case also our code gives results essentially identical to those obtained with Eq. 10.

We finally tested our iterative scheme, including the solution of both the flux conservative and Poisson equations, by considering a system that includes a charged surface bathed by a 1:1 electrolyte in the absence of $Ca^{2+}$ influx. The analytical solution of this system, derived by Gouy and Chapman (reviewed by McLaughlin (29)), is

$$V(z) = -2\frac{RT}{F}\ln\left(\frac{1 + \gamma e^{-z/\lambda_D}}{1 - \gamma e^{-z/\lambda_D}}\right), \quad (11)$$

with $\gamma = \dfrac{-2b/\lambda_D + \sqrt{\dfrac{4b^2}{\lambda_D^2} + 4}}{2}$, $b = \dfrac{2\varepsilon\varepsilon_0 RT}{F|\sigma|}$, and $\lambda_D = \sqrt{\dfrac{\varepsilon\varepsilon_0 RT}{2C_0F^2}}$, with ion concentrations related to the electrostatic potential by the Boltzmann equation

$$C_j = C_j^{\mathrm{bulk}} e^{-z_j FV(z)/RT}. \quad (12)$$

As shown in Fig. 1 *C* and *D*, in this case also our code recovered the solution given by the above-reported analytical expressions.

Finally, we checked the three-dimensional version of our iteration scheme by comparing its solution, obtained with only one open $Ca^{2+}$ channel, with that obtained with the two-dimensional iteration scheme (data not shown).

## Release model

A large variety of $Ca^{2+}$-triggered release models have been assessed experimentally and employed in modeling studies. Here we use a release model derived from $Ca^{2+}$ uncaging experiments at the rat calyx of Held synapse (15), including five independent $Ca^{2+}$ binding sites

$$X \underset{k_{\mathrm{off}}}{\overset{5k_{\mathrm{on}}[\mathrm{Ca}]}{\rightleftharpoons}} X\mathrm{Ca}_1 \underset{2k_{\mathrm{off}}}{\overset{4k_{\mathrm{on}}[\mathrm{Ca}]}{\rightleftharpoons}} X\mathrm{Ca}_2 \underset{3k_{\mathrm{off}}}{\overset{3k_{\mathrm{on}}[\mathrm{Ca}]}{\rightleftharpoons}} X\mathrm{Ca}_3 \underset{4k_{\mathrm{off}}}{\overset{2k_{\mathrm{on}}[\mathrm{Ca}]}{\rightleftharpoons}}$$
$$X\mathrm{Ca}_4 \underset{5k_{\mathrm{off}}}{\overset{k_{\mathrm{on}}[\mathrm{Ca}]}{\rightleftharpoons}} X\mathrm{Ca}_5 \underset{\delta}{\overset{\gamma}{\rightleftharpoons}} X\mathrm{Ca}_5^* \xrightarrow{\rho} F, \quad \text{(Scheme 4)}$$

where $k_{\mathrm{on}} = 3 \times 10^8\ \mathrm{M}^{-1}\ \mathrm{s}^{-1}$, $k_{\mathrm{off}} = 3000\ \mathrm{s}^{-1}$, $\gamma = 30{,}000\ \mathrm{s}^{-1}$, $\delta = 8000\ \mathrm{s}^{-1}$, and $\rho = 40{,}000\ \mathrm{s}^{-1}$. Since the $Ca^{2+}$ affinity of our release model (as for any other existing release model) was derived experimentally in terms of the $[\mathrm{Ca}]_{\mathrm{bulk}}$ under equilibrium conditions, it in fact represents an apparent $Ca^{2+}$ affinity, which in the presence of surface charges and with the $Ca^{2+}$ sensor located within the electrical double layer would differ significantly from the true $Ca^{2+}$ affinity. To overcome this problem, in our simulations we changed the $Ca^{2+}$ binding rate constant of the model ($k_{\mathrm{on}}$) to obtain an action-potential-induced release probability under control conditions of ~0.2, a value similar to that estimated at the rat calyx of Held synapse (9). The release probability of a vesicle, $P_r$, is defined as the probability that a vesicle resides in state $F$ at the end of a 5-ms computational time, starting from an initial condition where the vesicle resides in state $X$. During the computation, vesicle fusion is triggered by an action potential waveform obtained by using the following Hodgkin-Huxley equations (30):

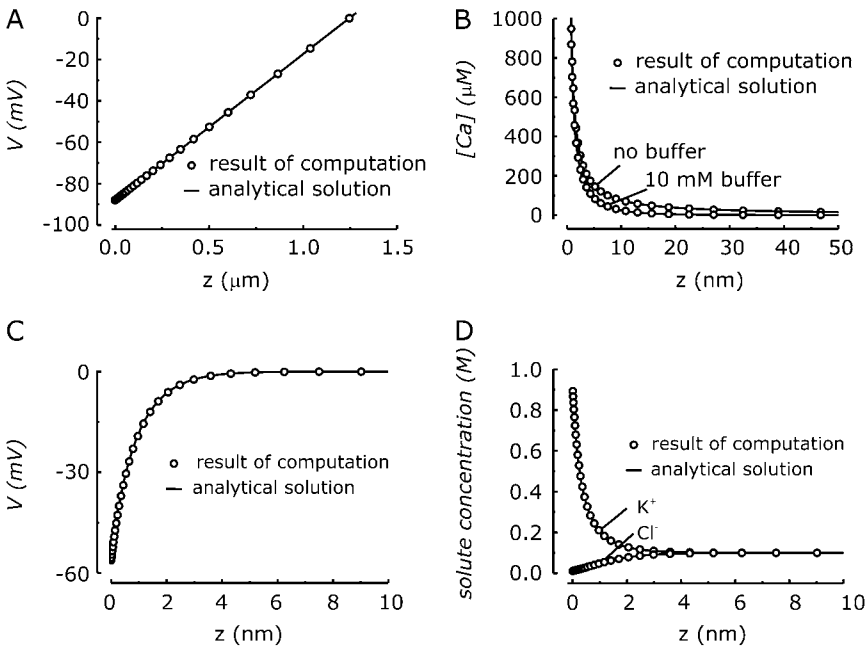


FIGURE 1 Comparison between existing analytical solutions (*solid lines*) and the output of our code (*open symbols*) for different simple systems. (*A*) A charged planar surface ($\sigma_T = -0.05\ \mathrm{C/m^2}$) with no ions in solution. (*B*) The flux conservative equation tested in the absence of buffer and with 10 mM of $Ca^{2+}$ buffer. (*C* and *D*) A 1:1 electrolytic solution in contact with a charged membrane ($\sigma_T = -0.05\ \mathrm{C/m^2}$).

$$C_m\frac{dV}{dt} = -g_{Na}m^3h(V-V_{Na}) - g_K n^4(V-V_K) - g_{Leak}(V-V_{Leak}) + I_{app}$$
$$\frac{dm}{dt} = \alpha_m(1-m) - \beta_m m,\ \frac{dh}{dt} = \alpha_h(1-h) - \beta_h h, \quad (13)$$
$$\frac{dn}{dt} = \alpha_n(1-n) - \beta_n n,$$

where $\alpha_m = 0.1\,(V+40)/(1-e^{V+40/10})$, $\beta_m = 4e^{-(V+65)/18}$, $\alpha_h = 0.07e^{-(V+65)/20}$, $\beta_h = 1/(1+e^{-(V+35)/10})$, $\alpha_n = 0.01(V+55)/(1-e^{-(V+55)/10})$, $C_m = 1\ \mu F/cm^2$, $g_{Na} = 120$ mS/cm$^2$, $g_K = 36$ mS/cm$^2$, $g_{Leak} = 0.3$ mS/cm$^2$, $V_{Na} = 50$ mV, $V_K = -77$ mV, and $V_{Leak} = -54$ mV. An action potential was induced by an applied current, $I_{app} = 30\ \mu A/cm^2$, of 1-ms duration.

In our model vesicle fusion is triggered by one $Ca^{2+}$ channel, described by the following two-state kinetic scheme (31,32)

$$C \underset{\beta}{\overset{\alpha}{\rightleftarrows}} O,$$

with $\alpha = 0.6 \times \exp(V/6)$ and $\beta = 0.2 \times \exp(-V/26.7)$. During the computation, the residence of each $Ca^{2+}$ channel in the open and closed state is determined using a Monte Carlo approach. Specifically, at each time step $\Delta t$ (1 $\mu$s), a random number is generated (*ran3* routine of Press et al. (25)) and the decision to accomplish the channel transition is made by comparing this number with the probability that a closed $Ca^{2+}$ channel opens (given by $\alpha\Delta t$) or the probability that an open $Ca^{2+}$ channel closes (given by $\beta\Delta t$). A similar approach was used to compute the state transitions of the release machinery, governed by Scheme 4. The release model we used assumes that after the $Ca^{2+}$ channel opens, the $Ca^{2+}$ sensor will instantaneously report the steady-state [Ca] produced by the $Ca^{2+}$ influx. This assumption is justified by previous theoretical studies showing that the steady-state [Ca] in close vicinity to an open $Ca^{2+}$ channel is reached within very short times (23).

## Parameters

Table 1 gives descriptions and numerical values for the parameters used in this study. The parameters $K_1$, $K_2$, and $K_3$, describing the equilibrium constants for ion binding to phospholipid membranes, were taken from studies assessing ion binding affinity to phosphatidylserine-containing membranes (18,24). As in Shahrezaei and Delaney (33), we considered an endogenous buffer with a rather high affinity, fast kinetics, and slow diffusion (34). We used 0.5 mM of this buffer, equivalent to a buffer capacity of 250. Total surface charge density ($\sigma_T$) was considered a variable parameter whose numerical values ranged between 0 and 0.1 C/m$^2$, in accordance with the surface charge densities found for the inner leaflet of mammalian plasma membrane (19). Finally, we considered a $Ca^{2+}$ current of 0.2 pA and a $Ca^{2+}$ diffusion coefficient of 220 $\mu m^2$/s. The sensitivity of the output of the model to variations of the main parameters is presented in Supplementary Material, Data S1.

**TABLE 1 Summary of parameters used**

| Description | Value |
|---|---|
| Equilibrium constant for $K^+$ binding to negatively charged phospholipids | $K_1 = 0.15\ M^{-1}$ |
| Equilibrium constant for $Ca^{2+}$ binding to negatively charged phospholipids | $K_2 = 12.0\ M^{-1}$ |
| Equilibrium constant for $Mg^{2+}$ binding to negatively charged phospholipids | $K_3 = 6.0\ M^{-1}$ |
| Bulk KCl concentration | [KCl] = 0.14 M |
| Bulk $CaCl_2$ concentration | [$CaCl_2$] = 1e-7 M |
| Bulk $MgCl_2$ concentration | [$MgCl_2$] = 0.5*e*–3 M |
| Total $Ca^{2+}$ buffer concentration | [$B_T$] = 0.5*e*–3 M |
| $Ca^{2+}$ association constant of the buffer | $k_1 = 3e8\ M^{-1}\ s^{-1}$ |
| $Ca^{2+}$ dissociation constant of the buffer | $k_{-1} = 600.0\ s^{-1}$ |
| Total membrane charge density | $\sigma_T = 0.0$ to $-0.1$ C/m$^2$ |
| $Ca^{2+}$ current throught the $Ca^{2+}$ channel | $i_{Ca} = 0$ to $-0.2$ pA |
| Valence of free buffer | $z_B = -2.0$ |
| Valence of $Ca^{2+}$-bound buffer | $z_{BCa} = 0.0$ |
| $Ca^{2+}$ ions diffusion coefficient | $D_{Ca} = 220\ \mu m^2/s$ |
| $Ca^{2+}$ buffer diffusion coefficient | $D_B = D_{Bca} = 27.5\ \mu m^2/s$ |

## RESULTS

### $Ca^{2+}$ microdomain profiles in the presence of membrane surface charge

Fig. 2 shows results obtained from simulations taken in the absence of $Ca^{2+}$ influx and with a membrane surface charge density of $-0.05$ C/m$^2$, a value comparable to those found for the inner leaflet of mammalian plasma membranes (19,29). The negative charge localized at the surface of the membrane generates a negative electrostatic potential that decays to near zero within a few nanometers from the membrane (Fig. 2 *A*). As shown in Fig. 2 *B*, this negative electrostatic potential causes an increase in the [Ca] near the membrane, according to the Boltzmann relationship valid under equilibrium conditions:

$$[Ca] = [Ca]_{bulk}\, e^{-z_{Ca}F\,V(z)/RT}, \quad (14)$$

where $[Ca]_{bulk}$ is the bulk $Ca^{2+}$ concentration, $z_{Ca}$ is the valence of $Ca^{2+}$ ions, $V(z)$ is the electrostatic potential at a distance $z$ from the membrane and $F$, $R$, and $T$ are the Faraday constant, the gas constant, and the absolute temperature, respectively. Fig. 2 *C* shows the relationship between the [Ca] at 0.1, 1, and 10 nm from the charged membrane and the $[Ca]_{bulk}$, built by making simulations in the presence of varying $[Ca]_{bulk}$. At a distance of 10 nm from the membrane, $[Ca] = [Ca]_{bulk}$, as expected from Eq. 14 for an electrostatic potential close to zero (cf. Fig. 1 *A*). By contrast, at distances of 0.1 and 1 nm from the membrane, the [Ca] is significantly higher than the $[Ca]_{bulk}$, as expected from the negative electrostatic potential present at these locations (cf. Fig. 2 *A* and Eq. 14). The [Ca] versus $[Ca]_{bulk}$ relationships for $z = 0.1$ and 1 nm end up being sublinear because of the significant binding of $Ca^{2+}$ ions to the negative membrane surface charge at the higher $[Ca]_{bulk}$ (which causes a sensible reduction of the net surface charge density, $\sigma$, and the electrostatic potential, $V$ (Fig. 2 *D*)).

Fig. 3 compares simulations of $Ca^{2+}$ microdomains obtained in the presence of an open $Ca^{2+}$ channel, when the membrane has no surface charge, and with a membrane carrying a surface charge of $-0.05$ C/m$^2$ and $-0.1$ C/m$^2$. Fig. 3 *A* shows the [Ca] profiles along the $z$ axis (normal to the membrane) at a radial distance of $r = 0$ (in front of the channel), and Fig. 3, *B–D*, shows the [Ca] profiles along the $r$ axis (parallel to the membrane) at distances of 0.1, 1, and 10 nm from the membrane. It is evident that inclusion of a negative surface charge significantly changes the [Ca] profiles. Very close to the membrane ($z = 0.1$ nm), the [Ca] is

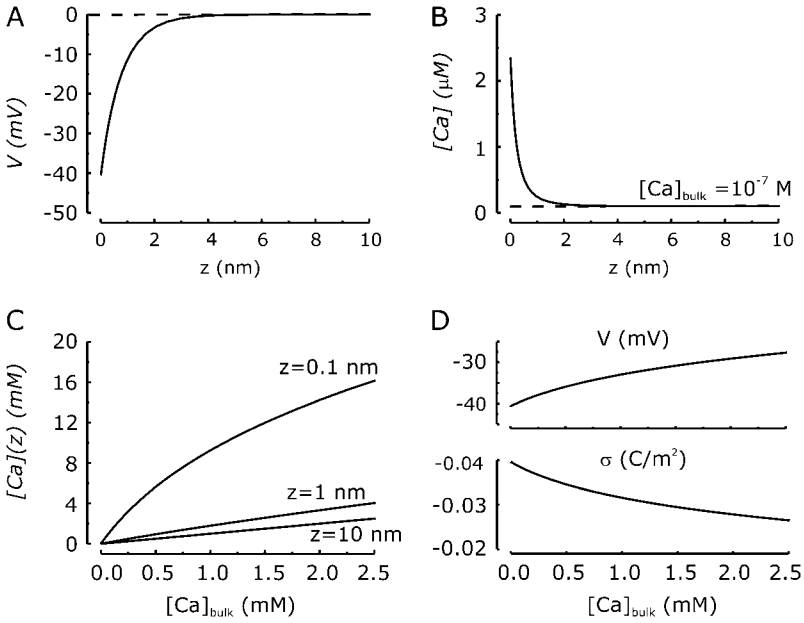


FIGURE 2 Diffuse double layer near a charged membrane in the absence of $Ca^{2+}$ influx. (*A*) Electrostatic potential ($V$) as a function of the distance from the membrane ($z$), obtained from a simulation carried out in the absence of $Ca^{2+}$ influx and with a membrane surface charge density of $-0.05$ C/m$^2$. (*B*) [Ca] as a function of distance from the membrane, obtained from the same simulation used in *A*. (*C*) Relationship between the [Ca] at 0.1, 1, and 10 nm from the membrane and $[Ca]_{bulk}$, obtained from a series of simulations carried out in the absence of $Ca^{2+}$ influx and with a surface charge density of $-0.05$ C/m$^2$. (*D*) Dependence of the effective (unbound) charge density ($\sigma$) and electrostatic potential ($V$ at $z = 0$) on the $[Ca]_{bulk}$, obtained from the same simulations used in *C*.

much higher in the presence of negative surface charges (Fig. 3 *B*) due to the strong attraction exerted by the negative electrostatic potential at these locations (Fig. 3 *B*, *inset*). Farther from the membrane, at $z = 1$ nm, the [Ca] in the presence of surface charge is still higher for relatively high radial distances from the channel (Fig. 3 *C*), in accordance with the existence of a still significantly negative electrostatic potential (Fig. 3 *C*, *inset*). However, at smaller distances from the $Ca^{2+}$ channel, the [Ca] estimated in the presence of surface charge is smaller than in the absence of surface charge. This result suggests that besides an obvious attractive tendency on $Ca^{2+}$ ions, surface charges exert an additional action that tends to reduce $Ca^{2+}$ accumulation near the point of $Ca^{2+}$ influx. This effect is even more evident by looking at the [Ca] profiles obtained at 10 nm from the membrane, where the electrostatic potential is decayed close to zero (Fig. 3 *D*, *inset*). In this case, the [Ca] in the presence of surface charge is lower than the [Ca] obtained without surface charge for radial distances from the channel $<\sim$40 nm. For higher radial distances, surface charges have only minor effects on the [Ca] (Fig. 3 *D*).

A possible explanation for the observed reduction in the [Ca] at small radial distances from the channel could be that a preferential surface diffusion of positively charged ions along the plane of the membrane is promoted by the negative surface charge (35,36). Surface charges would indeed favor $Ca^{2+}$ ions spreading out very efficiently along the lateral direction while allowing a much slower redistribution into

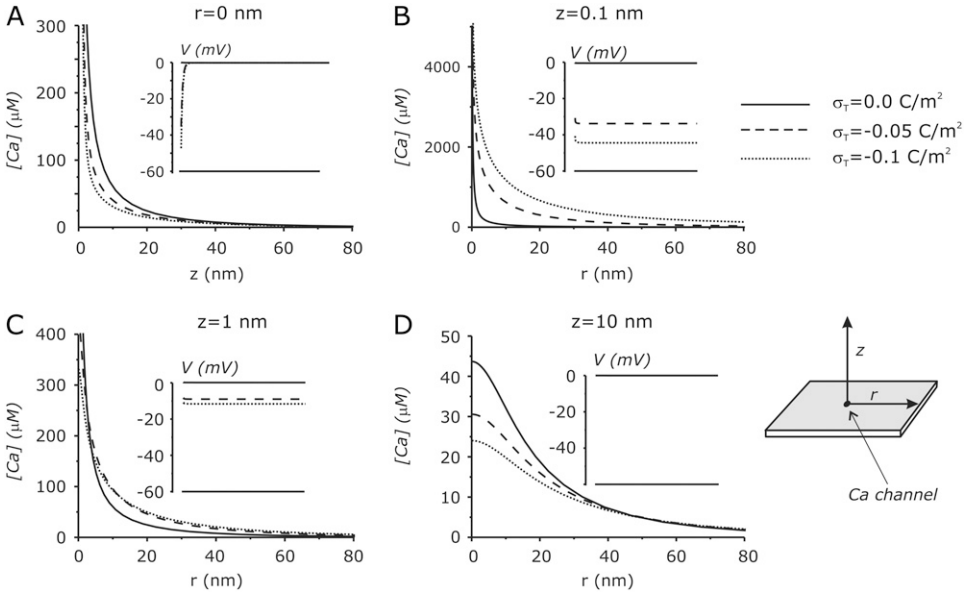


FIGURE 3 Effects of surface charge on the submembrane [Ca] profile in the presence of $Ca^{2+}$ influx. [Ca] profiles along the $z$ directions at $r = 0$ (*A*), and along the $r$ direction at 0.1, 1, and 10 nm from the membrane (*B–D*, respectively) for a diffusion model without surface charge (*solid lines*) and in the presence of surface charge densities of $-0.05$ and $-0.1$ C/m$^2$ (*dashed* and *dotted lines*, respectively). For all models, $i_{Ca} = -0.2$ pA. The insets show the spatial profiles of the electrostatic potential for the same simulations.

the third dimension normal to the membrane. To verify this hypothesis, we looked at the effects of surface charges on the electrodiffusive fluxes in both the lateral and normal directions. As shown in Fig. 4, the presence of surface charges markedly increases the lateral flux (estimated at the computational boxes in contact with the membrane) while producing a significant decrease of the electrodiffusive flux along the direction normal to the membrane (estimated for the computational boxes right in front of the channel). These results suggest that in the presence of surface charge, $Ca^{2+}$ ions preferentially travel along the lateral direction and very close to the membrane, thus reducing their accumulation at points more distant from the membrane.

## Effects of surface charge on the overlap of multiple $Ca^{2+}$ microdomains

To better understand the effects of surface charges on the spatial profile of the $Ca^{2+}$ microdomain, in Fig. 5 we plotted the [Ca] profiles of Fig. 3, normalized to the [Ca] present at 0.1 nm from the point of $Ca^{2+}$ influx. These plots suggest that a relevant effect of negative surface charges is to decrease the steepness of the $Ca^{2+}$ microdomain decay in the *r* direction, with the result that the [Ca] remains elevated for longer distances from the point of $Ca^{2+}$ influx (Fig. 5, *B–D*). By contrast, surface charges cause an increase in the steepness in the *z* direction, normal to the membrane (Fig. 5 *A*). The changes in the shape of $Ca^{2+}$ microdomains due to the presence of a surface charge can also be appreciated by the isoconcentration profiles shown in Fig. 5, *E* and *F*. It is evident that the $Ca^{2+}$ microdomain, symmetrically distributed along the *r* and *z* directions in the absence of surface charges, flattens out in the presence of negative surface charges.

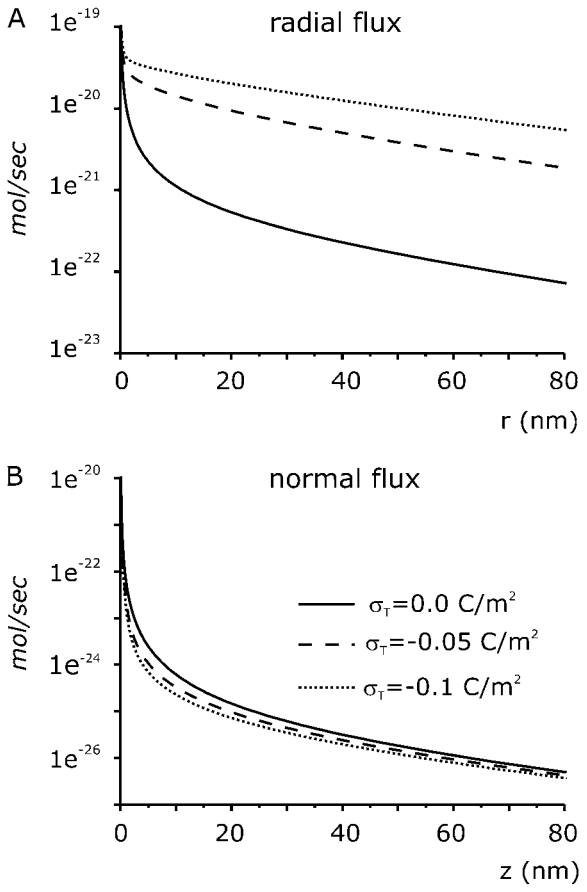


FIGURE 4 Changes of the Ca fluxes in the presence of surface charge. The electrodiffusive fluxes of $Ca^{2+}$ ions assessed (*A*) in the radial direction, at z = 0, and (*B*) along the direction normal to the membrane at the inner face of the channel ($r = 0$). The data are obtained from the same simulations presented in Fig. 3.

An interesting consequence of the reduced steepness of [Ca] profiles along the direction parallel to the membrane is an increased overlap of $Ca^{2+}$ microdomains originating from distinct $Ca^{2+}$ channels. This is better appreciated in the three-dimensional simulations shown in Fig. 6, where we consider six $Ca^{2+}$ channels (*1–6*) located 21 nm from each other (Fig. 6 *A*), and compare the [Ca] profiles near channel 1 when all six channels are open and when channels 2–6 are turned off (Fig. 6 *B*). This allows us to assess the contribution of neighbor channels to the $Ca^{2+}$ microdomain established by channel 1 (Fig. 6 *C*). As shown in Fig. 6, *B* and *C*, the contribution of channels 2–6 to the total [Ca] close to channel 1 is significantly increased when a negative surface charge is introduced, indicating an increased $Ca^{2+}$ microdomain overlap.

## Comparing the modeled $Ca^{2+}$ microdomain with experimental data

Experimental estimates of submembrane [Ca] near a point of $Ca^{2+}$ influx is usually performed by the so-called reverse approach (14,15,37). Specifically, the activity of $Ca^{2+}$-dependent proteins placed in close proximity to the site of $Ca^{2+}$ entry, such as $Ca^{2+}$-activated $K^+$ channels or the $Ca^{2+}$ sensor of the release machinery, is first evaluated in the absence of $Ca^{2+}$ influx, by applying different $[Ca]_{bulk}$s under equilibrium conditions. In the presence of $Ca^{2+}$ influx, the [Ca] reached at the sensor protein is then assumed to be equal to the $[Ca]_{bulk}$ that under equilibrium conditions (no $Ca^{2+}$ influx) would give the same degree of sensor protein activation, a quantity we here call apparent [Ca] at the sensor protein, $[Ca]_{SP*}$. Obviously, because of the $Ca^{2+}$ accumulation near a negatively charged membrane, for a sensor protein located very close to the membrane (where the electrostatic potential is still significantly negative (cf. Fig. 2)) the $[Ca]_{bulk}$ needed to attain a given protein activity (i.e., the $[Ca]_{SP*}$) will be lower than the actual [Ca] in contact with the sensor protein. It follows that the appropriate output of our model to be compared with experimental data deriving from the reverse approach is the $Ca^{2+}$ microdomain profile given in terms of the $[Ca]_{SP*}$. The converted $Ca^{2+}$ microdomain profiles, assessed from [Ca] versus $[Ca]_{bulk}$ relationships similar to those shown in Fig. 2 *C*, are shown in Fig. 7. These profiles indicate that the $[Ca]_{SP*}$ in the presence of a

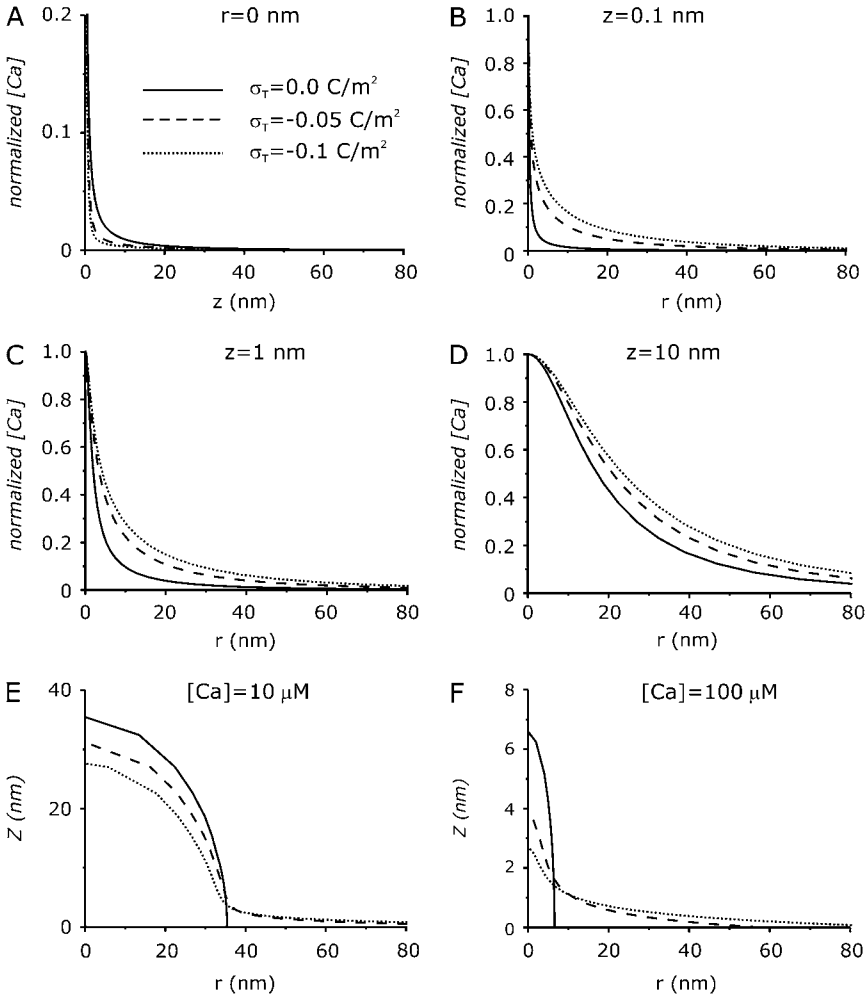


FIGURE 5 Effects of surface charges on the spatial profiles of the $Ca^{2+}$ microdomain. (*A–D*) Profiles of the [Ca] normalized to its value at 0.1 nm from the point of $Ca^{2+}$ influx, taken from the same simulation shown in Fig. 3. (*E* and *F*) Isoconcentration profiles around an open $Ca^{2+}$ channel obtained for [Ca]s of 10 $\mu$M and 100 $\mu$M, respectively, in the presence of surface charge densities of 0, $-0.05$, and $-0.1$ C/m$^2$.

surface charge is significantly smaller than the $[Ca]_{SP*}$ in the absence of a surface charge (obviously, in the absence of surface charge, $[Ca] = [Ca]_{SP*}$) for small distances from the channel, in both the $r$ and $z$ directions. At distances farther from the $Ca^{2+}$ channel, no substantial differences are observed in the $[Ca]_{SP*}$ profiles of the two models. These results indicate that membrane surface charges tend to reduce the estimated [Ca] at the sensor protein, provided that a strong $Ca^{2+}$ channel-vesicle colocalization exists.

## Effects of membrane surface charge on modeled synaptic release

The results shown above suggest that the presence of a surface charge at the inner leaflet of the membrane may have a significant effect on the vesicle release probability. To verify this notion, we used a $Ca^{2+}$-dependent release model, derived from experiments carried out on the calyx of Held (15), and looked at the effects of varying the membrane surface charge on the release probability. In these simulations, we assumed that the fusion of the vesicle is gated by only one $Ca^{2+}$ channel placed at a radial distance of either 10 or 40 nm from the vesicle $Ca^{2+}$ sensor. In the model, vesicle fusion is evoked by an action-potential-like voltage waveform that controls the gating of a two-state voltage-gated $Ca^{2+}$ channel (31). Since the $Ca^{2+}$ affinity of the release model we used (as for any other existing release model) was derived experimentally in terms of the $[Ca]_{bulk}$ under equilibrium conditions, it represents an apparent $Ca^{2+}$ affinity, which, in the presence of surface charges and with the $Ca^{2+}$ sensor located within the electrical double layer, may differ significantly from the true value. To overcome this problem, in our simulations we changed the $Ca^{2+}$ binding rate constant of the model ($k_{on}$) to obtain an action-potential-induced release probability under control conditions of ~0.2, a value similar to that estimated at the rat calyx of Held synapse (9). As shown in Fig. 8, we found that the effect of changing the surface charge density on the predicted neurotransmitter release varies depending on the position of the $Ca^{2+}$ sensor relative to the membrane. When the $Ca^{2+}$ sensor is placed very close to the membrane (i.e., within the electrical double layer), the evoked release probability increases with charge density. This is due to the increase of the [Ca] at these locations, promoted by the electrostatic attraction of $Ca^{2+}$ ions

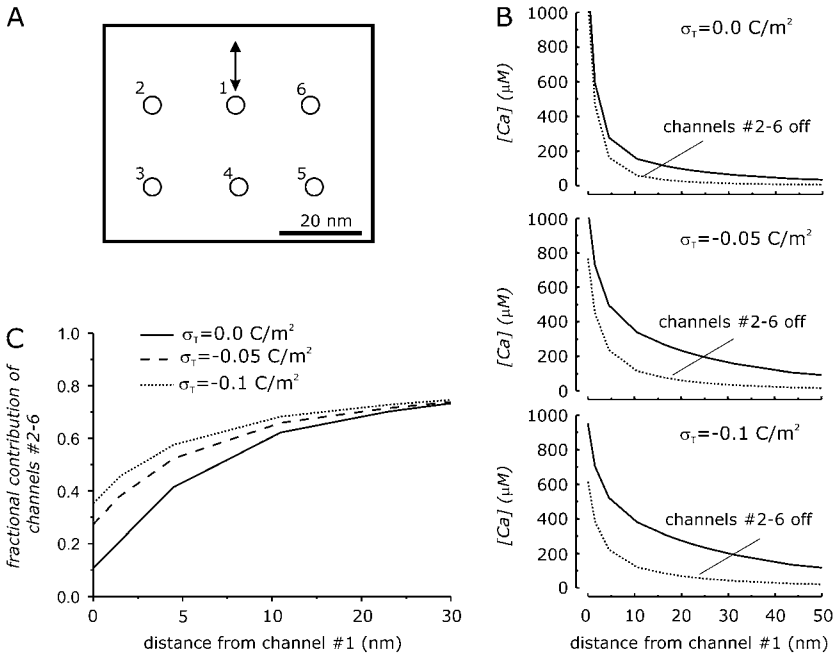


FIGURE 6 Effects of surface charge on $Ca^{2+}$ microdomain overlap. (*A*) Schematic representation of the $Ca^{2+}$ channel topography considered in our three-dimensional simulations. Circles indicate the positions of $Ca^{2+}$ channels, and the arrow indicates the direction where the [Ca] profiles shown in *B* and *C* were estimated. (*B*) [Ca] as a function of the distance from $Ca^{2+}$ channel 1 (cf. *A*) for three-dimensional simulations considering a surface charge density of 0, −0.05 and −0.1 C/m$^2$. The solid curves represent the [Ca] profiles obtained when all six $Ca^{2+}$ channels are open, whereas dotted curves represent the same profiles when only $Ca^{2+}$ channel 1 is open. (*C*) Fractional contribution of $Ca^{2+}$ channels 2–6 to [Ca] as a function of the distance from $Ca^{2+}$ channel 1 (cf. *A*).

by the negative surface charge (cf. Fig. 3). By contrast, an inverse relationship between the surface charge density and the evoked neurotransmitter release is obtained when the $Ca^{2+}$ sensor is located farther from the membrane (Fig. 8 *D*). As shown in Figs. 3 and 4, this is due to a reduction of the [Ca] at these locations caused by an increased lateral diffusion of $Ca^{2+}$ ions promoted by the surface charges.

## DISCUSSION

In this study, we looked at the effects of negative membrane surface charges on the properties of the $Ca^{2+}$ microdomains that build up around open $Ca^{2+}$ channels. We found that membrane surface charges, present at densities comparable to those found in the inner leaflet of plasma membranes, substantially modify the height and shape of the $Ca^{2+}$ microdomain. Specifically, besides an expected attractive tendency on $Ca^{2+}$ ions that results in an increased [Ca] very close to the membrane, surface charges exert an additional action that tends to reduce $Ca^{2+}$ build-up around open $Ca^{2+}$ channels. This causes a reduction in the [Ca] close to the point of $Ca^{2+}$ influx, an effect that is particularly evident at distances from the membrane >1 nm, where the electrostatic potential is low.

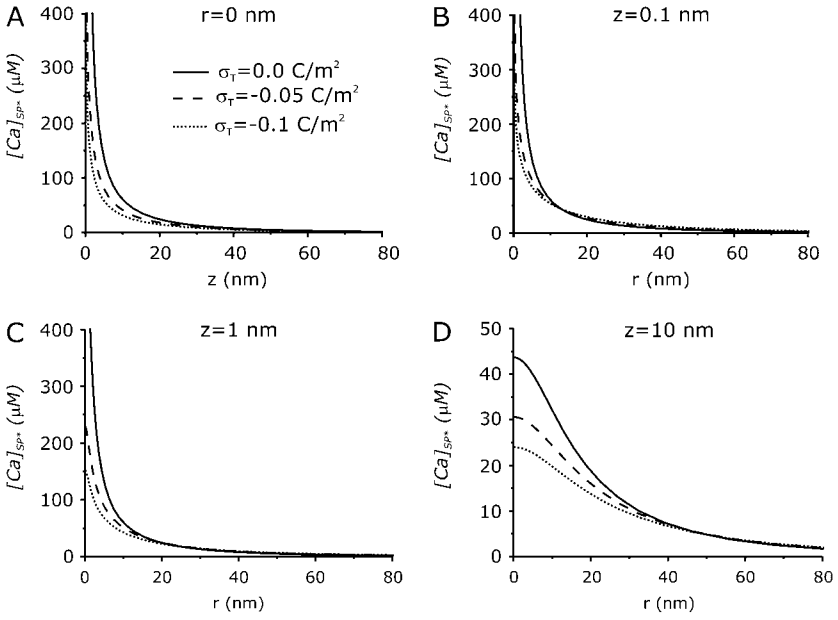


FIGURE 7 $[Ca]_{SP*}$ profiles at different surface charge densities. $[Ca]_{SP*}$ profiles along the *z* and *r* directions obtained from three different simulations considering a surface charge density of 0, −0.05, and −0.1 C/m$^2$.

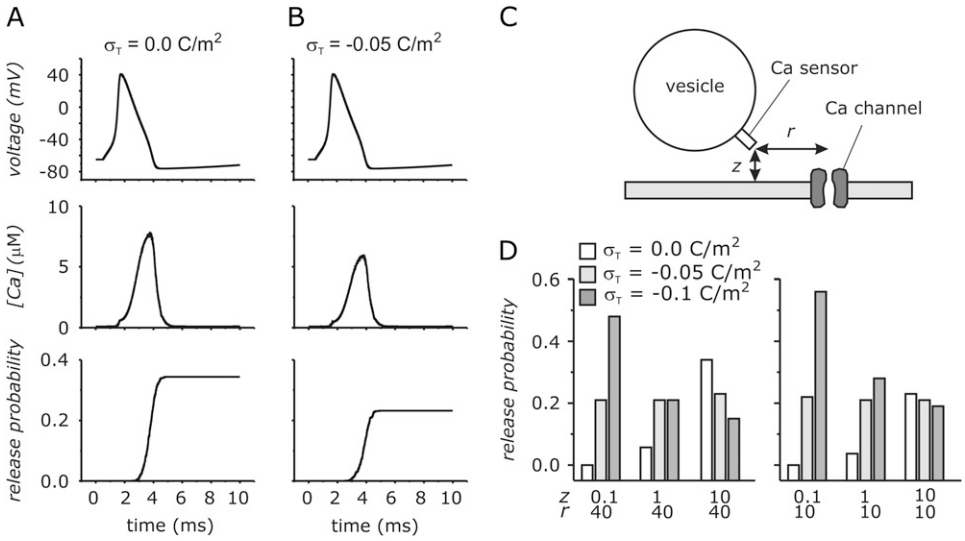


FIGURE 8 Effects of membrane surface charges on modeled synaptic release. (*A* and *B*) Temporal profile of the membrane potential, the [Ca], and the release probability obtained for a $Ca^{2+}$ sensor located at $r = 40$ nm and $z = 10$ nm, in the presence of a surface charge density of either 0 (*A*) or $-0.05$ C/m$^2$ (*B*). (*C*) Schematic representation of the model used to assess the effects of membrane surface charges on neurotransmitter release. (*D*) Release probability assessed from simulations similar to those shown in *A* and *B* for different locations of the $Ca^{2+}$ sensor and surface charge densities (indicated). For each location considered, the $Ca^{2+}$ binding rate constant to the $Ca^{2+}$ sensor was chosen to give a release probability of ~0.2 for a surface charge density of $-0.05$ C/m$^2$.

A possible explanation for this somehow unexpected result is that the negative surface charge facilitates lateral diffusion of the charged ions (35,36 (cf. Fig. 4)). $Ca^{2+}$ ions, attracted by the negative surface charges, raise the electrostatic potential in the vicinity of the channel, thus generating an electrical gradient that in turn increases the diffusion of $Ca^{2+}$ ions in the lateral direction. In this way, surface charges would enable a thin film of concentrated $Ca^{2+}$ to spread out very efficiently along the two dimensions of the surface membrane, rather than moving away from the membrane. Under this interpretation, electrostatics drastically change the properties of $Ca^{2+}$ diffusion away from the $Ca^{2+}$ channel, and clearly distinguish two distinct steps: a rapid lateral spread along the negative surface potential, and a slower redistribution of the spread $Ca^{2+}$ into the third dimension, normal to the membrane.

Our model also shows that negative surface charges tend to decrease the spatial steepness of the $Ca^{2+}$ microdomain, resulting in an increased overlap of microdomains originating from different $Ca^{2+}$ channels. This result suggests a greater contribution of distant $Ca^{2+}$ channels to the release of a vesicle located very close to a point of $Ca^{2+}$ influx. This could have particular relevance at synapses where vesicular release is controlled by multiple $Ca^{2+}$ channels, such as hippocampal and cerebellar synapses (17,38,39).

Another finding of this study is that surface charges reduce the [Ca] estimated at the release $Ca^{2+}$ sensor by a reverse approach, provided that a strong channel-vesicle colocalization exists. This revisitation would, for instance, make the estimated [Ca] at the $Ca^{2+}$ sensor of the calyx of Held synapse (10–25 $\mu$M, which is significantly lower than the previous theoretical predictions of 75–300 $\mu$M at few tens of nanometer from a $Ca^{2+}$ channel (7,8)) in principle not in contrast with a strong channel-vesicle colocalization.

We have also found that changing the surface charge density will have opposite effects on the action-potential-evoked neurotransmitter release, depending on the distance of the $Ca^{2+}$ sensor of the release machinery from the membrane. Specifically, if the $Ca^{2+}$ sensor lies within the electrical double layer, the release probability increases with the negative surface charge density. This is caused by the electrostatic attraction of $Ca^{2+}$ ions by the negative surface charges, which results in an increase of the [Ca] at these locations. By contrast, if the $Ca^{2+}$ sensor is located at farther distances from the membrane, an increase of the negative surface charge density causes a decrease of the release probability. As we have seen, this is due to the preferential lateral diffusion of $Ca^{2+}$ ions promoted by the surface charge, which results in a decrease of the [Ca] at locations relatively far from the membrane. Since experimental strategies to change the surface charge density are known (40), this theoretical prediction could be used to determine the distance of the $Ca^{2+}$ sensor from the membrane in real synapses.

Experimental data on the properties of $Ca^{2+}$ microdomains and neurotransmitter release are typically obtained from patched cells, using exogenous $Ca^{2+}$ buffers such as EGTA and BAPTA, which are considered to give information on the degree of colocalization of the Ca sensor and the point of Ca influx (1). These two $Ca^{2+}$ buffers have the same affinity for Ca ions, but BAPTA has a binding constant ~100 times larger than that of EGTA, thus allowing the capture of $Ca^{2+}$ ions in a very short time after their entry into the cytosol, and in this way reducing the [Ca] at points relatively close (<10 nm) to the Ca source. This kinetic difference between BAPTA and EGTA is due to the different protonation states of their $Ca^{2+}$ binding moieties at physiological pH, with EGTA almost totally protonated, whereas BAPTA shows a much lower pKa. In this respect, negative surface charges are expected to electrostatically attract protons close to the membrane, thus increasing the degree of protonation of BAPTA molecules close to the point of $Ca^{2+}$ influx, and reducing its $Ca^{2+}$ binding rate constant to values closer to those of EGTA. This effect could in theory explain a number

of experimental data showing that the $Ca^{2+}$ buffering capability of BAPTA, when compared to that observed for EGTA, is not as high as expected (17,41–43).

The predictions of our model suggest that changes in surface charge density could be instrumental in producing a form of activity-dependent change in release probability. Specifically, it is well known that aminophospholipid translocases, the enzymes that regulate the negatively charged phospholipid composition of the two sides of the plasma membrane, have an activity strongly regulated by the $[Ca]_i$ (44), such that a significant decrease of negatively charged phosphatidylserine present in the inner leaflet of plasma membrane can be observed after an increase in the $[Ca]_i$ (45). It is possible that changes in surface charge density are thus used to modulate neurotransmitter release in response to a strong $Ca^{2+}$ influx promoted by high-frequency neuronal stimulation.

We are aware that this model, based on a continuum approach that greatly simplifies the numerical calculus, has limitations. First, our model considers a homogeneous smeared surface charge density and a mean field approach for Ca ion diffusion. Although theoretical Poisson-Boltzmann calculations have shown that this approximation is realistic for physiologically relevant phospholipid compositions (22), at the smallest distance from the membrane considered in this article (0.1 nm), the mean field assumption could give results significantly different from the real case of discrete membrane negative charges. A more realistic view should include only a few Ca ions and discrete plasma membrane charges interacting with and influencing the diffusive movement. Second, a more realistic synaptic geometry should include membrane-associated synaptic vesicles, already shown to sensibly modify $Ca^{2+}$ diffusion near open $Ca^{2+}$ channels (33,46), as well as their cytoplasmic surface charge. It should in addition consider the narrow escape problem (47) resulting from the confined space between the plasma membrane and the vesicle. All these limitations call for a more appropriate approach, such as that provided by Monte Carlo simulations.

## SUPPLEMENTARY MATERIAL

To view all of the supplemental files associated with this article, visit www.biophysj.org.

We wish to thank Wolfgang Nonner (University of Miami) and Sandy Harper (University of Dundee) for useful comments on the manuscript.

This work was supported by grants from Fondazione Cassa di Risparmio di Perugia, Perugia, Italy.

## REFERENCES

1. Schneggenburger, R., and E. Neher. 2005. Presynaptic calcium and control of vesicle fusion. *Curr. Opin. Neurobiol.* 15:266–274.
2. Oheim, M., F. Kirchhoff, and W. Stuhmer. 2006. Calcium microdomains in regulated exocytosis. *Cell Calcium.* 40:423–439.
3. Stanley, E. F. 1997. The calcium channel and the organization of the presynaptic transmitter release face. *Trends Neurosci.* 20:404–409.
4. Seagar, M., and M. Takahashi. 1998. Interactions between presynaptic calcium channels and proteins implicated in synaptic vesicle trafficking and exocytosis. *J. Bioenerg. Biomembr.* 30:347–356.
5. Bajjalieh, S. 2001. SNAREs take the stage: a prime time to trigger neurotransmitter secretion. *Trends Neurosci.* 24:678–680.
6. Simon, S. M., and R. R. Llinas. 1985. Compartmentalization of the submembrane calcium activity during calcium influx and its significance in transmitter release. *Biophys. J.* 48:485–498.
7. Yamada, W. M., and R. S. Zucker. 1992. Time course of transmitter release calculated from simulations of a calcium diffusion model. *Biophys. J.* 61:671–682.
8. Roberts, W. M. 1994. Localization of calcium signals by a mobile calcium buffer in frog saccular hair cells. *J. Neurosci.* 14:3246–3262.
9. Meinrenken, C. J., J. G. Borst, and B. Sakmann. 2002. Calcium secretion coupling at calyx of Held governed by nonuniform channel-vesicle topography. *J. Neurosci.* 22:1648–1667.
10. Neher, E. 1998. Usefulness and limitations of linear approximations to the understanding of $Ca^{2+}$ signals. *Cell Calcium.* 24:345–357.
11. Augustine, G. J., E. M. Adler, and M. P. Charlton. 1991. The calcium signal for transmitter secretion from presynaptic nerve terminals. *Ann. N. Y. Acad. Sci.* 635:365–381.
12. Gentile, L., and E. F. Stanley. 2005. A unified model of presynaptic release site gating by calcium channel domains. *Eur. J. Neurosci.* 21:278–282.
13. Adler, E. M., G. J. Augustine, S. N. Duffy, and M. P. Charlton. 1991. Alien intracellular calcium chelators attenuate neurotransmitter release at the squid giant synapse. *J. Neurosci.* 11:1496–1507.
14. Schneggenburger, R., and E. Neher. 2000. Intracellular calcium dependence of transmitter release rates at a fast central synapse. *Nature.* 406:889–893.
15. Bollmann, J. H., B. Sakmann, and J. G. Borst. 2000. Calcium sensitivity of glutamate release in a calyx-type terminal. *Science.* 289:953–957.
16. Meinrenken, C. J., J. G. Borst, and B. Sakmann. 2003. Local routes revisited: the space and time dependence of the $Ca^{2+}$ signal for phasic transmitter release at the rat calyx of Held. *J. Physiol.* 547:665–689.
17. Borst, J. G., and B. Sakmann. 1996. Calcium influx and transmitter release in a fast CNS synapse. *Nature.* 383:431–434.
18. McLaughlin, S., N. Mulrine, T. Gresalfi, G. Vaio, and A. McLaughlin. 1981. Adsorption of divalent cations to bilayer membranes containing phosphatidylserine. *J. Gen. Physiol.* 77:445–473.
19. Olivotto, M., A. Arcangeli, M. Carla, and E. Wanke. 1996. Electric fields at the plasma membrane level: a neglected element in the mechanisms of cell signalling. *Bioessays.* 18:495–504.
20. Aoyagi, K., T. Sugaya, M. Umeda, S. Yamamoto, S. Terakawa, and M. Takahashi. 2005. The activation of exocytotic sites by the formation of phosphatidylinositol 4,5-bisphosphate microdomains at syntaxin clusters. *J. Biol. Chem.* 280:17346–17352.
21. McLaughlin, S., and D. Murray. 2005. Plasma membrane phosphoinositide organization by protein electrostatics. *Nature.* 438:605–611.
22. Peitzsch, R. M., M. Eisenberg, K. A. Sharp, and S. McLaughlin. 1995. Calculations of the electrostatic potential adjacent to model phospholipid bilayers. *Biophys. J.* 68:729–738.
23. Naraghi, M., and E. Neher. 1997. Linearized buffered $Ca^{2+}$ diffusion in microdomains and its implications for calculation of $[Ca^{2+}]$ at the mouth of a calcium channel. *J. Neurosci.* 17:6961–6973.
24. Eisenberg, M., T. Gresalfi, T. Riccio, and S. McLaughlin. 1979. Adsorption of monovalent cations to bilayer membranes containing negative phospholipids. *Biochemistry.* 18:5213–5223.
25. Press, W. H., S. A. Teukolsky, W. T. Vetterling, and B. P. Flannery. 1992. Numerical Recipes in C. Cambridge University Press, Cambridge, United Kingdom.

26. Nonner, W., and B. Eisenberg. 1998. Ion permeation and glutamate residues linked by Poisson-Nernst-Planck theory in L-type calcium channels. *Biophys. J.* 75:1287–1305.

27. Cardenas, A. E., R. D. Coalson, and M. G. Kurnikova. 2000. Three-dimensional Poisson-Nernst-Planck theory studies: influence of membrane electrostatics on gramicidin A channel conductance. *Biophys. J.* 79:80–93.

28. Hollerbach, U., D. P. Chen, and R. S. Eisenberg. 2001. Two- and three-dimensional Poisson-Nernst-Planck simulations of current flow through gramicidin A. *J. Sci. Comput.* 16:373–409.

29. McLaughlin, S. 1989. The electrostatic properties of membranes. *Annu. Rev. Biophys. Biophys. Chem.* 18:113–136.

30. Hodgkin, A. L., and A. F. Huxley. 1952. A quantitative description of membrane current and its application to conduction and excitation in nerve. *J. Physiol.* 117:500–544.

31. Bertram, R., G. D. Smith, and A. Sherman. 1999. Modeling study of the effects of overlapping $Ca^{2+}$ microdomains on neurotransmitter release. *Biophys. J.* 76:735–750.

32. Llinás, R., I. Z. Steinberg, and K. Walton. 1981. Presynaptic calcium currents in squid giant synapse. *Biophys. J.* 33:289–322.

33. Shahrezaei, V., and K. R. Delaney. 2004. Consequences of molecular-level $Ca^{2+}$ channel and synaptic vesicle colocalization for the $Ca^{2+}$ microdomain and neurotransmitter exocytosis: a Monte Carlo study. *Biophys. J.* 87:2352–2364.

34. Burrone, J., G. Neves, A. Gomis, A. Cooke, and L. Lagnado. 2002. Endogenous calcium buffers regulate fast exocytosis in the synaptic terminal of retinal bipolar cells. *Neuron.* 33:101–112.

35. Schumaker, M. F., and C. J. Kentler. 1998. Far-field analysis of coupled bulk and boundary layer diffusion toward an ion channel entrance. *Biophys. J.* 74:2235–2248.

36. Chan, D. Y., and B. Halle. 1984. The Smoluchowski-Poisson-Boltzmann description of ion diffusion at charged interfaces. *Biophys. J.* 46:387–407.

37. Roberts, W. M. 1993. Spatial calcium buffering in saccular hair cells. *Nature.* 363:74–76.

38. Wheeler, D. B., A. Randall, and R. W. Tsien. 1994. Roles of N-type and Q-type $Ca^{2+}$ channels in supporting hippocampal synaptic transmission. *Science.* 264:107–111.

39. Mintz, I. M., B. L. Sabatini, and W. G. Regehr. 1995. Calcium control of transmitter release at a cerebellar synapse. *Neuron.* 15:675–688.

40. Yeung, T., M. Terebiznik, L. Yu, J. Silvius, W. M. Abidi, M. Philips, T. Levine, A. Kapus, and S. Grinstein. 2006. Receptor activation alters inner surface potential during phagocytosis. *Science.* 313:347–351.

41. Kreiner, L., and A. Lee. 2006. Endogenous and exogenous $Ca^{2+}$ buffers differentially modulate $Ca^{2+}$-dependent inactivation of Ca(v)2.1 $Ca^{2+}$ channels. *J. Biol. Chem.* 281:4691–4698.

42. Mansvelder, H. D., and K. S. Kits. 1998. The relation of exocytosis and rapid endocytosis to calcium entry evoked by short repetitive depolarizing pulses in rat melanotropic cells. *J. Neurosci.* 18:81–92.

43. Borst, J. G., F. Helmchen, and B. Sakmann. 1995. Pre- and postsynaptic whole-cell recordings in the medial nucleus of the trapezoid body of the rat. *J. Physiol.* 489:825–840.

44. Williamson, P., L. Algarin, J. Bateman, H. R. Choe, and R. A. Schlegel. 1985. Phospholipid asymmetry in human erythrocyte ghosts. *J. Cell. Physiol.* 123:209–214.

45. Bitbol, M., P. Fellmann, A. Zachowski, and P. F. Devaux. 1987. Ion regulation of phosphatidylserine and phosphatidylethanolamine outside-inside translocation in human erythrocytes. *Biochim. Biophys. Acta.* 904:268–282.

46. Shahrezaei, V., and K. R. Delaney. 2005. Brevity of the $Ca^{2+}$ microdomain and active zone geometry prevent $Ca^{2+}$-sensor saturation for neurotransmitter release. *J. Neurophysiol.* 94:1912–1919.

47. Schuss, Z., A. Singer, and D. Holcman. 2007. The narrow escape problem for diffusion in cellular microdomains. *Proc. Natl. Acad. Sci. USA.* 104:16098–16103.